Modeling Surface Imperfections on Diffraction Gratings for the Extreme Ultraviolet

Ethan Edwards

A senior thesis submitted to the faculty of
Brigham Young University
in partial fulfillment of the requirements for the degree of

Bachelor of Science

R. Steven Turley, Advisor

Department of Physics and Astronomy

Brigham Young University

Copyright © 2021 Ethan Edwards

All Rights Reserved

ABSTRACT

Modeling Surface Imperfections on Diffraction Gratings for the Extreme Ultraviolet

Ethan Edwards
Department of Physics and Astronomy, BYU
Bachelor of Science

When the wavelength of light is comparable to the length scale of a surface's features, physical and geometrical optics approximations of reflectance fail. Since even the smoothest surfaces have nanometer-scale defects, finding direct methods for evaluating optical performance is critical in the extreme ultraviolet. One direct method for calculating reflectance uses the electric field integral equation (EFIE). In this project I use the EFIE to study how defects affect the far-field reflection of monochromatic plane-wave light from a one-dimensional blazed grating. Three defects were studied: uncorrelated and correlated ruling errors, and surface roughness. I examined effects on the resolving power (R) and efficiency (E) of a first-order diffraction peak. Considering 0.2 wavelengths of RMS error in each case, I found that roughness decreased R by 0.4% and E by 94.5%, uncorrelated ruling errors decreased R by 0.0% and E by 1.3%, and correlated ruling errors decreased R by 4.4% and E by 32.0%.

Keywords: Extreme Ultraviolet, Reflectance, Mirror, Roughness, Diffraction Grating, EFIE, Gaussian Quadrature, XUV

ACKNOWLEDGMENTS

I am very grateful for the support and guidance of my advisor, Dr. Turley. Without his encouragement and assistance I would not have been able to accomplish this project. I am also grateful for Dr. Allred, who recruited me into his and Dr. Turley's research group. I appreciate the financial support I have received from the College of Physical and Mathematical Sciences, which enabled me to pursue research without incurring debt. Finally, I wish to thank my family for their enthusiasm and unwavering confidence in me.

Contents

Table of Contents iv

List of Figures vi

List of Tables vi

1 Background 1
1.1 Extreme Ultraviolet . . . 1
1.2 Previous Work . . . 2
1.3 Diffraction Gratings . . . 4
1.3.1 Operation . . . 4
1.3.2 Measures of Performance . . . 6
1.4 Scope of Project . . . 6
1.5 Electric Field Integral Equation . . . 7
1.5.1 Maxwell's Equations . . . 7
1.5.2 Wave Equation . . . 8
1.5.3 Helmholtz Equation . . . 8
1.5.4 Electric Field Integral Equation . . . 10
1.6 Matrix Equation . . . 10
1.6.1 Perfect Conductor . . . 11
1.6.2 Green's Function of the Helmholtz Equation . . . 11
1.6.3 Line Integration . . . 11
1.6.4 Quadrature Rule . . . 12

2 Methods 14
2.1 Incident Wave . . . 14
2.2 Surface Discretization . . . 15
2.2.1 Nonsingular Quadrature Rule . . . 15
2.2.2 Singular Quadrature Rule . . . 16
2.3 Surface Generation . . . 17
2.3.1 Surface Roughness . . . 17
2.3.2 Ruling Errors . . . 20

2.4 Solving the Matrix Equation 21
2.5 Far-field Reflectance 22

3 Results and Conclusions **23**
3.1 Results 23
3.1.1 Surface Roughness 24
3.1.2 Uncorrelated Ruling Error 25
3.1.3 Correlated Ruling Error 28
3.2 Thresholds 30
3.2.1 Thresholds in Wavelengths 30
3.2.2 Application to EUV 31
3.3 Discussion 32
3.4 Future Work 32
3.5 Conclusion 34

Appendix A Calculating *R* **35**

Appendix B Choosing the Number of Points Across a Surface **39**

Bibliography **44**

Index **46**

List of Figures

1.1 Reflection grating 5

2.1 Evaluation points along a patch 15
2.2 AFM thin film image 19
2.3 PSDF of thin film cross-section 20

3.1 R_r for surface roughness 24
3.2 E_r for surface roughness 25
3.3 R_r for uncorrelated ruling error 26
3.4 E_r for uncorrelated ruling error 27
3.5 R_r for correlated ruling error 28
3.6 E_r for correlated ruling error 29

A.1 $|1-R/R_i| \leq 0.01$ 37
A.2 $|1-R/R_i| \leq 0.01$ 38

B.1 Re{J} at 4 pts per wavelength 40
B.2 Re{J} at 8 pts per wavelength 41
B.3 Re{J} at 16 pts per wavelength 42

List of Tables

3.1 Thresholds for efficiency in λ 30

3.2 Thresholds for efficiency at $\lambda = 86$ nm 31

B.1 First-order peak width. Surfaces were modeled at five points per λ. 43

Chapter 1

Background

1.1 Extreme Ultraviolet

Reflective surfaces have many applications in the sciences. Astronomers use highly reflective mirrors to collect light of all wavelengths in their study of the cosmos. Spectroscopy, which probes the composition and structure of matter with light, often uses reflective surfaces called gratings to break up light into individual frequencies for analysis. Lasers, which are practically ubiquitous in modern society, often rely on a highly reflective optical cavity to contain light and provide optical feedback.

One challenge to producing reflective surfaces of high quality is surface defects. Defects change surface geometry, causing unwanted scattering and degrading performance. The severity of a defect is dependent on its size relative to incident wavelength; therefore, as incident wavelength decreases scattering becomes harder to control. My project involves quantifying the degradation which occurs as defect size increases relative to incident wavelength. Specifically, I will introduce defects of varying relative size to a diffraction grating and compute its intensity profile to determine effects on performance.

Recently, interest has grown for studying the reflective properties of surfaces in the extreme ultraviolet (EUV). This has been spurred in part by potential applications for astronomy and EUV lithography. One uniquely challenging aspect of producing reflective surfaces for use in the EUV is that of surface defects. Since EUV wavelengths span roughly from 100nm to 10nm, even small defects may cause considerable scattering. Since an understanding of how defects affect performance is important to the EUV community, I will apply my results to a diffraction grating for use in the EUV. In this study I frequently reference code which I developed with the help of my advisor, Dr. Turley. All of the code developed for this project may be found on the BYU Department of Physics and Astronomy's GitLab account under the project ReflectRough.

1.2 Previous Work

Scalar correction factors such as the Debye-Waller and Nevot-Croce factors have been used in the past to account for surface roughness [1,2]. These factors have had some success in predicting the effect of roughness.

Deriving the Debye-Waller factor starts by assuming that light in vacuum strikes an interface made up of a random superposition of lattice vibrations [2]. This interface causes reflections of different period and phase to interfere, leading to a Gaussian distribution for reflectivity r:

$$r(z) = \frac{r_0}{\sigma\sqrt{2\pi}} \exp\left[-z^2/(2\sigma^2)\right] \tag{1.1}$$

where σ represents the RMS roughness of a surface. Taking the Fourier transform of this distribution:

$$r(q) = \int_{-\infty}^{\infty} r(z) e^{-iqz} dz \tag{1.2}$$

$$= r_0 e^{-q^2\sigma^2/2} \tag{1.3}$$

where $q = \frac{4\pi}{\lambda} n \sin\theta$ represents the transfer of momentum. Note that λ is the vacuum wavelength of the incident light, n is the material index of refraction, and θ is the angle measured clockwise from

grazing. The reflected intensity $R(q)$ is obtained by squaring $r(q)$:

$$R(q) = R_0 e^{-q^2\sigma^2}. \tag{1.4}$$

The exponential in Equation 1.4 is the Debye-Waller factor .

Nevot and Croce introduced one correction to Equation 1.4. Since interactions at an interface necessarily involve two indices n_1 and n_2 and two propagation angles θ_1 and θ_2, they replaced q^2 in the Debye-Waller factor with a geometric average $q_1 q_2$ resulting in

$$R(q) = R_0 e^{-q_1 q_2 \sigma^2} \tag{1.5}$$

In the 1980's work done by D.G. Stearns at Lawrence Livermore National Labs resulted in a more generalized model of reflectance [3]. His work, which describes interfaces as transition layers of varying relative permittivity ε_r, offers several distinct advantages over other models. His formulation applies to any arbitrary surface structure, including rough, diffuse and nonhomogeneous interfaces; it does not constrain the extent of an interface; it applies at any angle; and it accounts for absorbing media.

Many other scientists have extended roughness models to multilayers . For example, in a paper by Wang *et al.*, specular reflection from a rough single layer was modeled by the equation [4]

$$I = \left| \left(\frac{\rho_s - \rho_f}{\rho_s} \right) e^{-q^2\sigma_s^2} + \frac{\rho_f}{\rho_s} e^{-q^2\sigma_f^2} e^{iqd} \right|^2 I_F \tag{1.6}$$

where I is the specular reflected intensity and I_F is the Fresnel intensity of the substrate. The quantities ρ_s and ρ_f represent substrate and thin film electron density, respectively; q represents the momentum transfer used in Equation 1.4; σ_s and σ_f represent the roughness of the substrate and thin film; and d is thin film thickness. Equation 1.6 reveals that intensity oscillates with varying thin film thickness d but that as σ_f increases the oscillations damp out. Experimental evidence by Wang *et al.* confirmed this prediction.

Many of these models include assumptions which do not hold in the EUV. For one, roughness is often assumed to be small in comparison to the incident wavelength. Second, these correction

factors were developed for X ray scattering, where scattering is often weak for any interface [3, 5]. Finally, the models assume that non-specular scattering does not couple back into specular scattering. For these reasons I will instead calculate reflectance from a surface directly using the Electric Field Integral Equation (EFIE). This method works in all regimes, at any level of scattering, and it makes no assumptions.

1.3 Diffraction Gratings

1.3.1 Operation

One of the important reflectors used in the EUV is a diffraction grating. Diffraction gratings allow scientists to break up light into its various components. Gratings work either by allowing light to transmit through small slits or by allowing light to reflect off a grooved surface. Since I model the latter type of grating, I will explain how a reflection grating works. The following explanation uses geometrical optics to simplify the concepts.

In Figure 1.1, coherent and collimated light comes in at an angle θ_i (measured clockwise from the grating parallel) and reflects off the surface of a blazed grating. The blazed grating has periodic grooves spaced a distance d apart and teeth that slope upward at an angle θ_B, called the blaze angle. Consider two rays of light that strike the surface a horizontal distance d apart. When the rays reflect from the surface they will have traveled different optical path lengths. Their path length difference is $d(\cos\theta_i + \cos\theta_r)$. If this difference is some integer multiple m of λ, these rays will interfere constructively; if their path difference is some half-integer multiple $m + \frac{1}{2}$ of λ, the rays will interfere destructively. In mathematical form, then,

$$m\lambda = d(\cos\theta_i + \cos\theta_r) \text{ (constructive interference)} \tag{1.7}$$

$$(m + \frac{1}{2})\lambda = d(\cos\theta_i + \cos\theta_r) \text{ (destructive interference).} \tag{1.8}$$

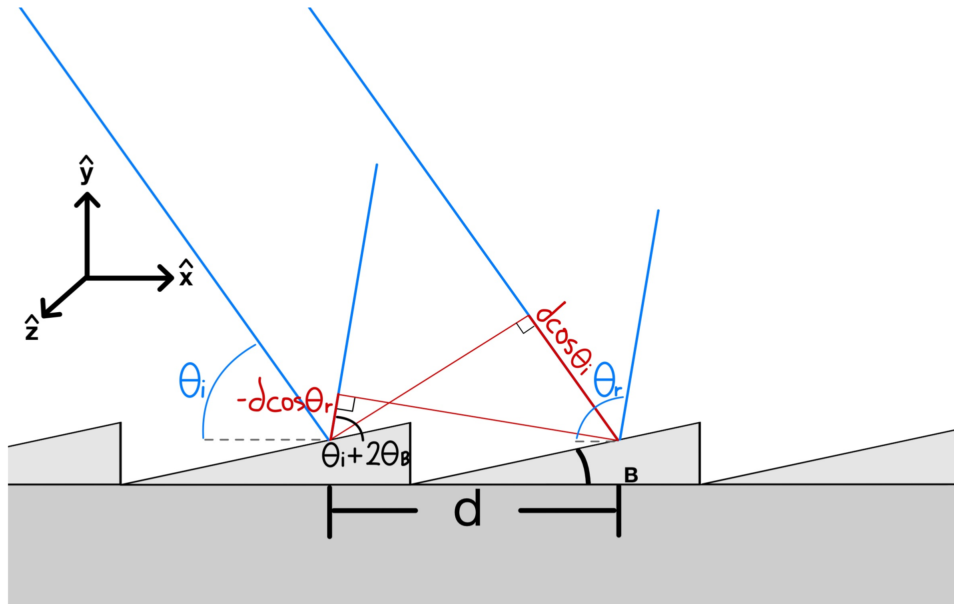

Figure 1.1 The angle of diffraction peak

When light incident at an angle θ_i strikes a grating with groove spacing d, we want to know the angles for which reflection is a maximum. If $m = 0$, we see from Eq. 1.7 that

$$\cos\theta_i = -\cos\theta_r \tag{1.9}$$

$$\cos\theta_i = \cos(\pi - \theta_r) \tag{1.10}$$

which is Snell's law. For $m \neq 0$ we can rearrange Eq. 1.7 to show θ_r as a function of m and λ:

$$\theta_r = \arccos\left(\frac{m\lambda}{d} - \cos\theta_i\right). \tag{1.11}$$

This equation describes the angular distribution of maxima and minima from a blazed grating. Angles θ_r of maximum intensity corresponding to a path length difference $m\lambda$ are called mth order peaks. Since θ_r is dependent on λ, scientists cane use diffraction gratings to isolate a wavelength of interest.

1.3.2 Measures of Performance

In this project I focus on two measures of performance: efficiency E and resolving power R . Efficiency relates the intensity of a peak of interest to the total reflected intensity and ranges from zero to one. Resolving power, defined as $\frac{\lambda}{\Delta\lambda}$, describes how well the diffraction grating separates wavelengths; it quantifies the uncertainty of any measured wavelength.

1.4 Scope of Project

For this project I calculate the efficiency and resolving power of blazed gratings with defects and compare their performance to an ideal grating. The initial setup of each reflectance problem is the same. Monochromatic plane-wave light strikes a perfectly-conducting one-dimensional blazed surface at 45° measured clockwise from the grating parallel. Using the Electric Field Integral Equation, I am able to determine the surface current J which generates a reflected electric field. Using J I find the far-field angular distribution of reflected intensities due to the S-polarized field and calculate the efficiency and resolving power of the first-order diffraction peak.

Measuring length in units of optical wavelength λ, the ideal surface has 250 teeth (249 grooves) spaced 7.9λ apart giving a surface 19750 wavelengths wide. I then modify the ideal surface to include one of three defects: surface roughness, uncorrelated ruling errors, or correlated ruling errors. Surface roughness is random deviation in the normal vector of an ideal surface and may be quantified with a root mean square (RMS) height σ_r. Ruling errors are errors in the location of a groove on a grating surface. Details on each type of defect is found in Section 2.3. Defects are characterized by the parameters σ_r, σ_u amd σ_c, which determine the RMS error for a defect. Although the defects are assumed to be random in nature, the parameters σ_r, σ_u and σ_c allow me to generate surfaces with a specific RMS value for each given defect. After generating a sample of 50 surfaces with some non-zero value of σ_r, σ_u or σ_c, I estimate the average E and R for a population

of surfaces with equal RMS error and compare these values to the efficiency E_i and resolving power R_i of the ideal grating. To facilitate this, I use relative efficiency E_r and relative resolving power R_r, defined as the ratios of E to E_i and of R to R_i. Using E_r and R_r elucidates the effect of defects on grating performance.

1.5 Electric Field Integral Equation

In classical electrodynamics, the Electric Field Integral Equation (EFIE) relates an electric current density $\mathbf{J}$ with its generated electric field $\mathbf{E}$. Understanding how the geometry of a surface affects its reflective properties requires solving the EFIE for $\mathbf{J}$. In this section I will derive the EFIE from Maxwell's equations; the following section focuses on using it to find $\mathbf{J}$.

1.5.1 Maxwell's Equations

Maxwell's equations form the theoretical basis for classical electromagnetism. In differential form, Maxwell's equations are

$$\nabla \cdot \mathbf{E} = \frac{\rho}{\varepsilon_0} \tag{1.12}$$

$$\nabla \cdot \mathbf{B} = 0 \tag{1.13}$$

$$\nabla \times \mathbf{E} = -\frac{\partial \mathbf{B}}{\partial t} \tag{1.14}$$

$$\nabla \times \mathbf{B} = \mu_0 \mathbf{J} + \mu_0 \varepsilon_0 \frac{\partial \mathbf{E}}{\partial t}. \tag{1.15}$$

In these equations $\mathbf{E}$ represents the electric field, $\mathbf{B}$ represents the magnetic field, ρ is charge density, $\mathbf{J}$ is current density, ε_0 is vacuum permittivity and μ_0 is vacuum permeability.

1.5.2 Wave Equation

I am interested in finding a solution to Maxwell's equations that describes wavelike behavior for the electric field. In particular, I am interested in finding a solution that describes an electric field propagating in vacuum. Following the work done by Thevenin [6], I will rewrite Eq. 1.14 and take its curl

$$\nabla \times \nabla \times \mathbf{E} + \frac{\partial}{\partial t}(\nabla \times \mathbf{B}) = 0 \tag{1.16}$$

Using the vector identity $\nabla \times (\nabla \times \mathbf{A}) = \nabla(\nabla \cdot \mathbf{A}) - \nabla^2 \mathbf{A}$, the previous equation becomes

$$\nabla(\nabla \cdot \mathbf{E}) - \nabla^2 \mathbf{E} + \frac{\partial}{\partial t}(\nabla \times \mathbf{B}) = 0 \tag{1.17}$$

Replacing $\nabla \cdot \mathbf{E}$ using Eq. 1.12 and $\nabla \times \mathbf{B}$ using Eq. 1.15 gives

$$\nabla(\frac{\rho}{\varepsilon_0}) - \nabla^2 \mathbf{E} + \mu_0 \frac{\partial \mathbf{J}}{\partial t} + \mu_0 \varepsilon_0 \frac{\partial^2 \mathbf{E}}{\partial t^2} = 0 \tag{1.18}$$

Assuming the medium of propagation is vacuum, $\rho = 0$ and $\mathbf{J} = \mathbf{0}$. Switching the sign and recalling that $c \equiv \frac{1}{\sqrt{\mu_0 \varepsilon_0}}$ gives the wave equation in its usual form

$$\nabla^2 \mathbf{E} - \frac{1}{c^2} \frac{\partial^2 \mathbf{E}}{\partial t^2} = 0. \tag{1.19}$$

1.5.3 Helmholtz Equation

The Helmholtz equation is a time-independent form of the wave equation describing radiation from a source that propagates out to infinity. This describes reflection, in which currents on a conducting surface generate a field that propagates out to infinity. The Helmholtz equation may be derived using separation of variables. Assume the time-dependent electric field may be expressed as a

product of two functions, one of space and one of time: $\mathbf{E} = \mathbf{E}_i(\mathbf{r})T(t)$

$$\nabla^2 \mathbf{E}_i T - \frac{1}{c^2}\mathbf{E}_i \frac{\partial^2 T}{\partial t^2} = 0 \tag{1.20}$$

Divide each term by $\mathbf{A}(\mathbf{r})T(t)$

$$\frac{\nabla^2 \mathbf{E}_i}{\mathbf{E}_i} - \frac{1}{c^2 T}\frac{\partial^2 T}{\partial t^2} = 0 \tag{1.21}$$

Note that both terms are equal for all values of $\mathbf{r}$ and t. This is true if and only if both terms are constant. Assume that both terms are equal to $-k^2$

$$\frac{\nabla^2 \mathbf{E}_i}{\mathbf{E}_i} = -k^2 \tag{1.22}$$

$$\frac{1}{Tc^2}\frac{\partial^2 T}{\partial t^2} = -k^2 \tag{1.23}$$

Since I am not interested in time-dependency, I can drop the second equation from consideration and focus on Equation 1.22:

$$\nabla^2 \mathbf{E}_i = -k^2 \mathbf{E}_i \tag{1.24}$$

$$\nabla^2 \mathbf{E}_i + k^2 \mathbf{E}_i = 0 \tag{1.25}$$

Since I will be working with $\mathbf{E}_i$ exclusively, I can suppress the subscript on it as long as I remember that $\mathbf{E}$ represents the time-independent electric field. Continuing thus and factoring $\mathbf{E}$ in Equation 1.25 gives

$$(\nabla^2 + k^2)\mathbf{E} = 0. \tag{1.26}$$

Equation 1.26 is the Helmholtz Equation. The variable k represents the wavenumber. In general form, $k = \sqrt{\mu\varepsilon}\omega$; however, since the electric waves are propagating in vacuum, μ becomes μ_0 and ε becomes ε_0 so that $k = \frac{\omega}{c}$.

1.5.4 Electric Field Integral Equation

In my problem the surface current **J** generates an electric field which satisfies the nonhomogeneous Helmholtz Equation; that is,

$$(\nabla^2 + k^2)\mathbf{E} = \mathbf{J}. \tag{1.27}$$

I want to know the field **E** generated by **J**; mathematically, this means solving for **E**. This can be done by taking the convolution of **J** and **G**, the Green's function of the Helmholtz equation. The Green's function of the Helmholtz equation

$$(\nabla^2 + k^2)\mathbf{G}(\mathbf{r}) = -\delta(\mathbf{r}) \tag{1.28}$$

describes how a system which obeys the Helmholtz Equation responds to an impulse. Equation 2.65 in Johnson's thesis gives an expression for the z-component of **E** in terms of **J** and **G** [7]. I will make two modifications. First, I will replace A_z with Equation 2.47 in his thesis. Second, I will set K_t to zero; this term is defined from the magnetic field strength **H** and will be ignored in this study [8]:

$$\mathbf{E}(\mathbf{r}) = (\mathbf{G} * J)(\mathbf{r}) = -ik\eta \int \mathbf{J}(\mathbf{r}')\mathbf{G}(\mathbf{r} - \mathbf{r}')d\mathbf{r}' \tag{1.29}$$

where k is the wave number (recall that $k = 2\pi$ in units of wavelengths) and $\eta = \sqrt{\mu/\varepsilon}$. For convenience, I will absorb the factor $ik\eta$ into **J**. Equation 1.29 is known as the Electric Field Integral Equation (EFIE) . In order to understand how surface geometry affects reflection, I must solve the EFIE for **J**.

1.6 Matrix Equation

The variable I wish to solve for is inside an integral. In most cases, including this one, finding an analytic solution for **J** is not possible. Instead, I can obtain a numerical solution by converting the

EFIE into a matrix equation. Up to this point I have only made a few assumptions, but moving forward I will make more assumptions to simplify and contextualize the problem.

1.6.1 Perfect Conductor

In Equation 1.29 $\mathbf{J}$ generates an electric field $\mathbf{E}$. In the context of this problem $\mathbf{E}$ is the reflected field, which I will denote as $\mathbf{E_{ref}}$. Since the grating is assumed to be a perfect conductor, the total electric field is 0. Noting that $\mathbf{E_{tot}} = \mathbf{E_{inc}} + \mathbf{E_{ref}}$ it follows that

$$\mathbf{E_{ref}} = -\mathbf{E_{inc}}. \tag{1.30}$$

1.6.2 Green's Function of the Helmholtz Equation

Electromagnetic waves generated on the grating surface will propagate outward in the xy-plane. Therefore, the Green's function used must be for the 2D-Helmholtz equation. In two dimensions (and recalling that units of distance are in wavelength), the Green's function for the Helmholtz equation is [7]

$$\mathbf{G}(\mathbf{r} - \mathbf{r}') = \frac{i}{4} H_0^{(1)}(2\pi|\mathbf{r} - \mathbf{r}'|) \tag{1.31}$$

where $\mathbf{r}$ is the observation point (x, y), $\mathbf{r}'$ is the source point (x', y'), and $H_0^{(1)}$ is the zero-order Hankel function of the first kind.

1.6.3 Line Integration

With these modifications in place, Eq. 1.29 becomes

$$\mathbf{E}_{inc}(\mathbf{r}) = \int_C \mathbf{J}(\mathbf{r}')\mathbf{G}(\mathbf{r} - \mathbf{r}')d\mathbf{r}' \tag{1.32}$$

which is integrated along the grating surface. Here $\mathbf{E}_{inc}(\mathbf{r})$ denotes the incident electric field at a point $\mathbf{r}$ and the variable of integration $\mathbf{r}'$ denotes source points where $\mathbf{J}(\mathbf{r}')$ contributes to the

observed electric field. To evaluate Equation 1.32, I can use a line integral across the surface. Let dx' and dy' represent infinitesimals along source coordinates x' and y', respectively. How far along the surface do I move when going from x' to $x + dx'$? Using the Pythagorean theorem, I would move a distance

$$\sqrt{dx'^2 + \left(\frac{dy'}{dx'}\right)^2 dx'^2}, \tag{1.33}$$

where $\left(\frac{dy'}{dx'}\right)$ is the slope at x'. Then

$$\mathbf{E}_{inc}(\mathbf{r}) = \int \mathbf{J}(\mathbf{r}')\mathbf{G}(\mathbf{r}-\mathbf{r}')\sqrt{dx'^2 + \left(\frac{dy'}{dx'}\right)^2 dx'^2} \tag{1.34}$$

$$\mathbf{E}_{inc}(\mathbf{r}) = \int \mathbf{J}(\mathbf{r}')\mathbf{G}(\mathbf{r}-\mathbf{r}')\sqrt{1 + \left(\frac{dy'}{dx'}\right)^2} dx'. \tag{1.35}$$

Note that in the line integral y' is a function of x', and therefore integration over just x' is allowed.

1.6.4 Quadrature Rule

Now that $\mathbf{E}_{inc}$ and $\mathbf{G}(\mathbf{r}-\mathbf{r}')$ are known and the integral is defined correctly, only solving for $\mathbf{J}(\mathbf{r}')$ remains. To find $\mathbf{J}(\mathbf{r}')$ the integral must be discretized using a quadrature rule (examples of quadrature rules are the Riemann sum, which is a zero-order rule; the first-order trapezoidal rule; and the second-order Simpson's Method). While higher-order rules produce better approximations, they require many evaluation points and are computationally expensive. In an effort to preserve both accuracy and efficiency, the bounds of integration are separated into n patches, and each patch is integrated using a third-order quadrature rule. Such a rule requires four evaluation points along each patch and will be exact inasmuch as $\mathbf{J}$ may be represented by a third-order polynomial over any patch-length region ℓ.

With n patches each requiring four evaluation points, the integral across the surface requires $4n$ source points. However, the Green's function includes two points–the observation point $\mathbf{r}$ and the source point $\mathbf{r}'$. For this problem, I chose the observation points to be at the same locations as the

source points. This means the integral requires $4n$ total evaluations; furthermore, it means that $\mathbf{E}_{inc}$ will become a vector with $4n$ elements. Let E_i be the electric field evaluated at the observation point x_i and let x_j represent a source point. Then

$$E_i = \sum_{j=1}^{4n} J_j w_j G_{ij} \tag{1.36}$$

where w_j is a product of the weights of integration c_j and the line integral term $\sqrt{1+\left(\frac{dy'}{dx'}\right)^2}$. Let $Z_{ij} = w_j G_{ij}$. Then

$$E_i = \sum_{j=1}^{4n} J_j Z_{ij}. \tag{1.37}$$

Let E be a vector containing each E_i, J be a vector containing each J_j, and Z be a matrix (called the impedance matrix) containing each Z_{ij}. With this notation in place,

$$E = ZJ \tag{1.38}$$

where E and J are $4n$-element vectors and Z is a $4n \times 4n$ matrix. I can solve for J by multiplying both sides of Equation 1.38 by the inverse of Z. I describe how I calculate Z^{-1} in Section 2.4.

Chapter 2

Methods

2.1 Incident Wave

The coordinate system chosen is given in Figure 1.1. Assuming symmetry about the z-axis effectively reduces the scattering surface to one dimension. The surface lies on the x-axis centered at the origin. Section 1.4 describes the light source for each surface modeled; here I will write out the incident wave in mathematical form.

Using complex notation a plane wave takes the form $\mathrm{Re}\{e^{i(\vec{k}\cdot\vec{r}-\omega t)}\}$ where $\vec{k}$ is the wave vector, $\vec{r}$ is the position vector, ω is angular frequency and t is time. Following standard notation, I will suppress $\mathrm{Re}\{\}$ and let it be implicit. Assuming time independence, the incident wave is of the form $e^{i(\vec{k}\cdot\vec{r})}$. Recalling that distance is measured in units of wavelength, let $\vec{k} = 2\pi(\cos\theta_i\hat{\imath} - \sin\theta_i\hat{\jmath})$, where θ_i is the incident angle. For each test $\theta_i = 45°$; therefore $\vec{k}\cdot\vec{r}$ becomes $\sqrt{2}\pi(x-y)$ and the plane wave becomes $e^{\sqrt{2}\pi i(x-y)}$.

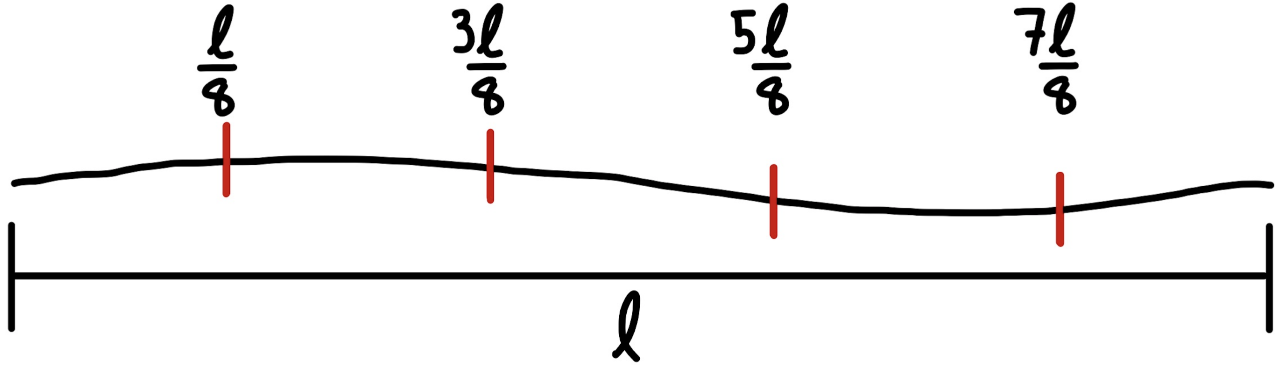

Figure 2.1 Evaluation points along a patch of length ℓ

2.2 Surface Discretization

In Section 1.5, I discretized the EFIE into a matrix equation which may be solved for J. To do so, I followed Johnson's method and separated the surface integral into n patches of integration using a third-order quadrature rule [7]. The quadrature rule requires four weights c_j which I left underived. In this section I will derive the weights to be used.

Letting the observation points be at the same location as the source points causes some integrals to have singularities; specifically, integrating over patches containing observation points. In these integrals, when $x_i = x_j$ the Hankel function (Equation 1.31) has an argument of zero, which returns a complex infinity. Thus a separate set of weights must be used to integrate over patches with an observation point. I will therefore introduce separate weights for nonsingular and singular patches.

2.2.1 Nonsingular Quadrature Rule

Let ℓ be the length of a patch and choose four equally spaced evaluation points at $\frac{\ell}{8}$, $\frac{3\ell}{8}$, $\frac{5\ell}{8}$, and $\frac{7\ell}{8}$, measured from the beginning of the patch. An example of this is depicted in Figure 2.1. The general equation for the rule is then

$$c_1 f\left(\frac{\ell}{8}\right) + c_2 f\left(\frac{3\ell}{8}\right) + c_3 f\left(5\frac{\ell}{8}\right) + c_4 f\left(7\frac{\ell}{8}\right) = A \tag{2.1}$$

As mentioned in Section 1.4, I want this rule to allow exact integration over a patch of all functions up to third-order polynomials; as such, it will satisfy the following equations:

$$c_1 + c_2 + c_3 + c_4 = \int_0^\ell dx \tag{2.2}$$

$$c_1\left(\frac{\ell}{8}\right) + c_2\left(\frac{3\ell}{8}\right) + c_3\left(\frac{5\ell}{8}\right) + c_4\left(\frac{7\ell}{8}\right) = \int_0^\ell x dx \tag{2.3}$$

$$c_1\left(\frac{\ell}{8}\right)^2 + c_2\left(\frac{3\ell}{8}\right)^2 + c_3\left(\frac{5\ell}{8}\right)^2 + c_4\left(\frac{7\ell}{8}\right)^2 = \int_0^\ell x^2 dx \tag{2.4}$$

$$c_1\left(\frac{\ell}{8}\right)^3 + c_2\left(\frac{3\ell}{8}\right)^3 + c_3\left(\frac{5\ell}{8}\right)^3 + c_4\left(\frac{7\ell}{8}\right)^3 = \int_0^\ell x^3 dx \tag{2.5}$$

Solving this system of equations yields

$$c_1 = \frac{13\ell}{48} \tag{2.6}$$

$$c_2 = \frac{11\ell}{48} \tag{2.7}$$

$$c_3 = \frac{11\ell}{48} \tag{2.8}$$

$$c_4 = \frac{13\ell}{48} \tag{2.9}$$

Since these integrals are linear operators, the weights c_j will allow exact integration for any patch which may be represented by a cubic polynomial $f(x) = ax^3 + bx^2 + cx + d$.

2.2.2 Singular Quadrature Rule

When integrating over a patch containing an observation point, the Green's function will have a singularity. The constants derived above will not work for these patches, so another quadrature rule must be developed. Jedediah Johnson [7] derived these weights in his paper, and I will give the result here. Let ℓ be the length of a patch, and choose four equally spaced evaluation points at $\frac{\ell}{8}$, $\frac{3\ell}{8}$,

$\frac{5\ell}{8}$, and $\frac{7\ell}{8}$. Then

$$c_1 = \frac{1}{48}[105W_1 - 142W_2 + 60W_3 - 8W_4] \tag{2.10}$$

$$c_2 = \frac{1}{16}[-35W_1 + 94W_2 - 52W_3 + 8W_4] \tag{2.11}$$

$$c_3 = \frac{1}{16}[21W_1 - 62W_2 + 44W_3 - 8W_4] \tag{2.12}$$

$$c_4 = \frac{1}{48}[-15W_1 + 46W_2 - 36W_3 + 8W_4] \tag{2.13}$$

where

$$W_n \equiv \left(\frac{4}{\ell}\right)^n \int_{\text{patch}} x^n G(x_i, x) dx. \tag{2.14}$$

2.3 Surface Generation

As described in Section 1.4, I generated grating imperfections by modifying the ideal surface to include some RMS error in either surface roughness, uncorrelated ruling error or correlated ruling error. Here I will outline the methods used to generate these imperfect surfaces.

2.3.1 Surface Roughness

To correctly model surface roughness, I imitated characteristics seen in the atomic force microscope (AFM) images of thin film surfaces observed in the Allred-Turley lab. Figure 2.2 shows an AFM image of a sample thin film from the Allred-Turley lab. Using a data visualization program called Gwyddion, I was able to study features of the surface.

One statistic I obtained was the RMS roughness of the surface. Gwyddion defines the one-dimensional RMS surface roughness as

$$\sqrt{\frac{1}{N}\sum_{j=1}^{N} x_j^2} \tag{2.15}$$

where N is the number of surface samplings and x_j is the height of the surface and is defined to average to zero [9]. For the surface in Figure 2.2, for example, the RMS roughness was 2.24 nm.

Another statistic I used was the one-dimensional power spectral density function (PSDF) of a cross section of the surface in Figure 2.2. Signal analysts often use the PSDF of stochastic signals to analyze their behavior in the frequency domain. The PSDF may be applied not only to electrical signals, but to any abstract signal. Let $f(x)$ represent surface height as a function of location on a cross-sectional strip of some surface. Then $f(x)$ is a random function. It will be beneficial to define a truncated form of $f(x)$ as

$$f_X(x) = f(x)w_X(x) \tag{2.16}$$

where $w_X(x)$ is a unit window function with a period of X centered about x_0. The (abstract) energy of this random function may be defined as [10]

$$E = \int_{x_0-X/2}^{x_0+X/2} |f(x)|^2 dx = \int_{-\infty}^{\infty} |f_X(x)|^2 dx \tag{2.17}$$

The average power P is then

$$P = \frac{1}{X}\int_{-\infty}^{\infty} |f_X(x)|^2 dx = \frac{1}{X}\int_{-\infty}^{\infty} |F_X(k)|^2 dk \tag{2.18}$$

by Parseval's theorem, where $F_X(k)$ is the Fourier transform of $f_X(x)$. To get the average power in the case of an untruncated process, let $X \to \infty$

$$P = \lim_{X\to\infty} \frac{1}{X}\int_{-\infty}^{\infty} |F_X(k)|^2 dk. \tag{2.19}$$

Define

$$S_{xx}(k) = \lim_{X\to\infty} \frac{1}{X}|F_X(k)|^2, \tag{2.20}$$

then

$$P = \int_{-\infty}^{\infty} S_{xx}(k)dk. \tag{2.21}$$

Note that the units of $S_{xx}(k)$ must be power per frequency; in other words, Equation 2.20 defines the power spectral density function (PSDF). Equation 2.20 reveals that $S_{xx}(k) \propto F(k)$. Intuitively, this

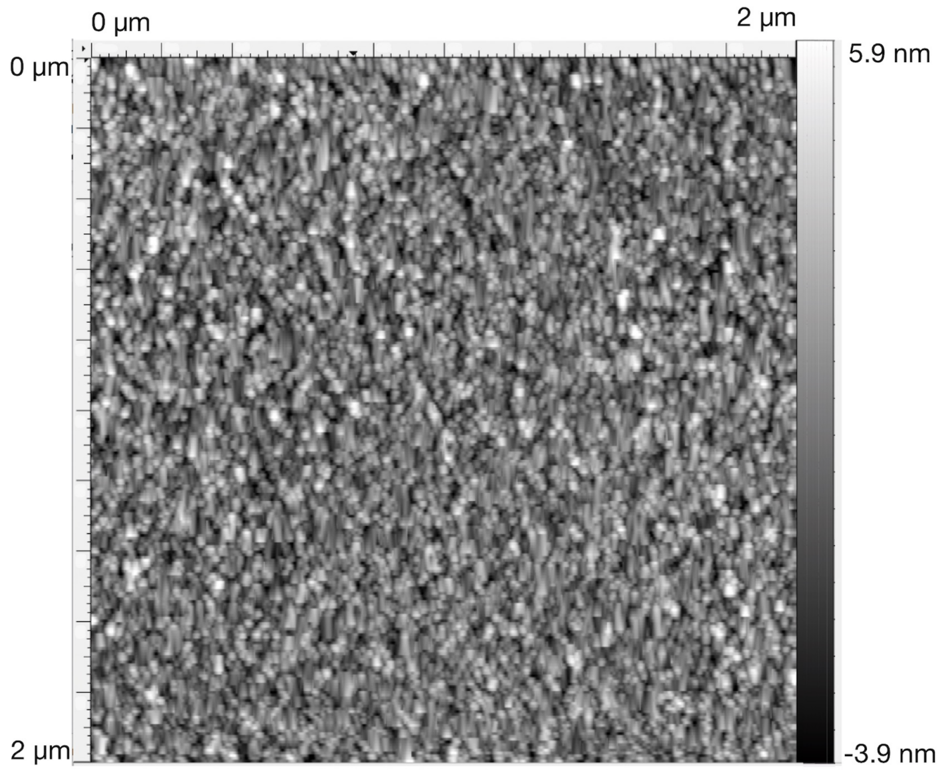

Figure 2.2 AFM image of a thin film from the Allred-Turley lab

means that surface roughness can be thought of as a random signal across a surface composed of spatial frequencies with varying intensities; the PSDF gives the relative intensities of these spatial frequencies.

Figure 2.3 is the PSDF of a cross section of the surface sampled in Figure 2.2. As you can see, the PSDF looks like a Gaussian distribution of spatial frequencies centered about zero. To imitate this, I generated a list of random values centered around zero with a standard deviation of one, transformed the list to obtain spatial frequencies, then used a Gaussian filter function to match the trend of spatial frequency amplitudes seen in Figure 2.3. For this study I used a standard deviation of $\sigma = 2\pi$ on the Gaussian filter function, which translates to a standard deviation of one optical wavelength for spatial frequencies. I then took the inverse transform of the filtered frequencies to obtain a one-dimensional list of heights. Finally, I multiplied the list by a constant to obtain a

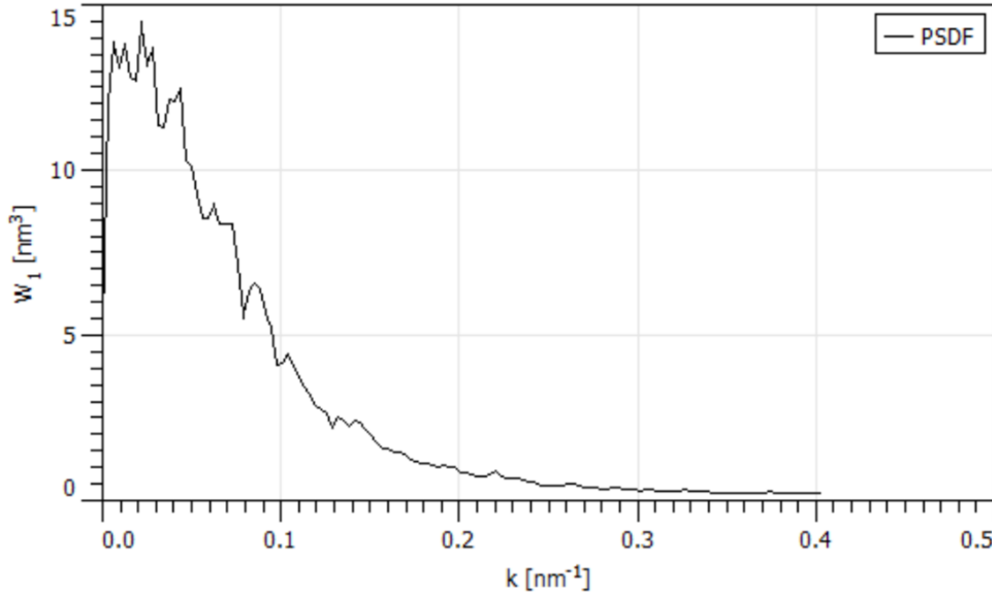

Figure 2.3 A cross-sectional PSDF of the surface in Figure 2.2 reveals an approximate normal distribution of spatial frequencies

desired RMS value and added this list element-wise to the list of surface heights for the ideal blazed grating.

2.3.2 Ruling Errors

To describe ruling errors I will define the location of the *n*th groove on an ideal grating as x_n and let d be the ideal spacing between adjacent grooves. Uncorrelated ruling errors occur when the location of groove n is given by

$$\xi_n = x_n + \varepsilon_u \tag{2.22}$$

where ε_u is a random number taken from a normal distribution centered at the origin with a standard deviation σ_u. Correlated ruling errors occur when the location of groove n is given by

$$\xi_n = \xi_{n-1} + d + \varepsilon_c \tag{2.23}$$

where ε_c is defined similarly to ε_u. These equations show that error propagates in the case of correlated ruling errors and does not propagate for uncorrelated ruling errors.

Recognizing that the parameter varied for ruling errors is the standard deviation σ, one may question whether σ actually represents the RMS error. I will show that this is the case using a generic random variable ε from a normal distribution $f(\varepsilon)$ centered about 0

$$f(\varepsilon) = \frac{1}{\sigma\sqrt{2\pi}} e^{-\varepsilon^2/2\sigma^2}. \tag{2.24}$$

The RMS value of the random variable ε_{RMS} is the square root of the expectation value of ε^2:

$$\varepsilon_{RMS} = \sqrt{\int_{-\infty}^{\infty} \varepsilon^2 f(\varepsilon) d\varepsilon} \tag{2.25}$$

$$= \frac{1}{\sqrt[4]{\sigma^2 2\pi}} \sqrt{\int_{-\infty}^{\infty} \varepsilon^2 e^{-\varepsilon^2/2\sigma^2} d\varepsilon} \tag{2.26}$$

$$= \frac{1}{\sqrt[4]{\sigma^2 2\pi}} \sqrt{\sqrt{2\pi}\sigma^3} \tag{2.27}$$

$$= \sigma. \tag{2.28}$$

2.4 Solving the Matrix Equation

Various techniques may be used to solve Eq. 1.38. In this project I used Julia's built-in matrix solver. In this problem Z is a non-triangular square matrix, so Julia uses an LU factorization method [11]. Each surface was generated with 19748 points, which corresponds to 10 points per wavelength and leads to a 19748×19748 impedance matrix. Justification for this is found in Appendix B.

2.5 Far-field Reflectance

Once J has been determined, it can be used to find the reflected electric field. Johnson [7] derived an equation for determining the far-field reflectance. While his equation expresses a more general problem, ignoring surface magnetization (and recalling that J has absorbed $ik\eta$) leads to the form

$$E(\phi) = \frac{e^{i(kr+\pi/4)}}{2\sqrt{2\pi kr}} \int_C J(x', y') e^{2i\pi(cos(\phi)x' - sin(\phi)y')} ds' \tag{2.29}$$

Here r represents distance from the origin and ϕ is the observation angle measured clockwise from grazing. To solve this integral, I use the same quadrature rule as the one developed for generating the matrix equation. Since this equation has no singularities, only the nonsingular weights need to be used. I also do not care about dependence on r; therefore, I will integrate along a semicircle a distance r from the origin. I am interested in finding the normalized intensity profile, which is given by

$$I(\phi) = \frac{|E(\phi)|^2}{I_0} \tag{2.30}$$

where $I_0 = \sin\theta_i |E_{inc}(\phi)|^2$. The $\sin\theta_i$ is necessary to account for changes in incident intensity due to incident angle θ_i (intuitively, incident intensity is greatest when $\theta_i = \frac{\pi}{2}$ and lowest as θ_i approaches 0).

The far-field distribution I contains the angular width $\Delta\phi$ of the $m = 1$ order peak; however, in order to calculate resolving power R the quantity $\Delta\lambda$ must be determined. I review the steps for determining $\Delta\lambda$ from $\Delta\phi$ in Appendix A.

Chapter 3

Results and Conclusions

3.1 Results

Now that I've developed methods to compute reflectance from various surface geometries I can model the effect of surface defects on grating performance. As I explained in Section 1.4, my aim is to understand how efficiency E and resolving power R is affected when increasing surface roughness, uncorrelated ruling errors or correlated ruling errors. To do so I computed the performance of an ideal grating at the first order diffraction peak then added surface defects and re-computed the performance for comparison. In this section I plot the relative efficiency E_r and relative resolving power R_r as a function of increased RMS error. Since these errors are random, each data point (except the point representing the ideal surface) represents an average of 50 surfaces with equal RMS error. Along with each data point I plot the standard error of the mean (SEM). The SEM is defined as

$$SEM = \frac{\sigma}{\sqrt{n}} \tag{3.1}$$

where σ represents the standard deviation of the sample set and n is the sample size. The SEM is an estimate of where the population mean may be, and thus gives a quantitative measure of uncertainty.

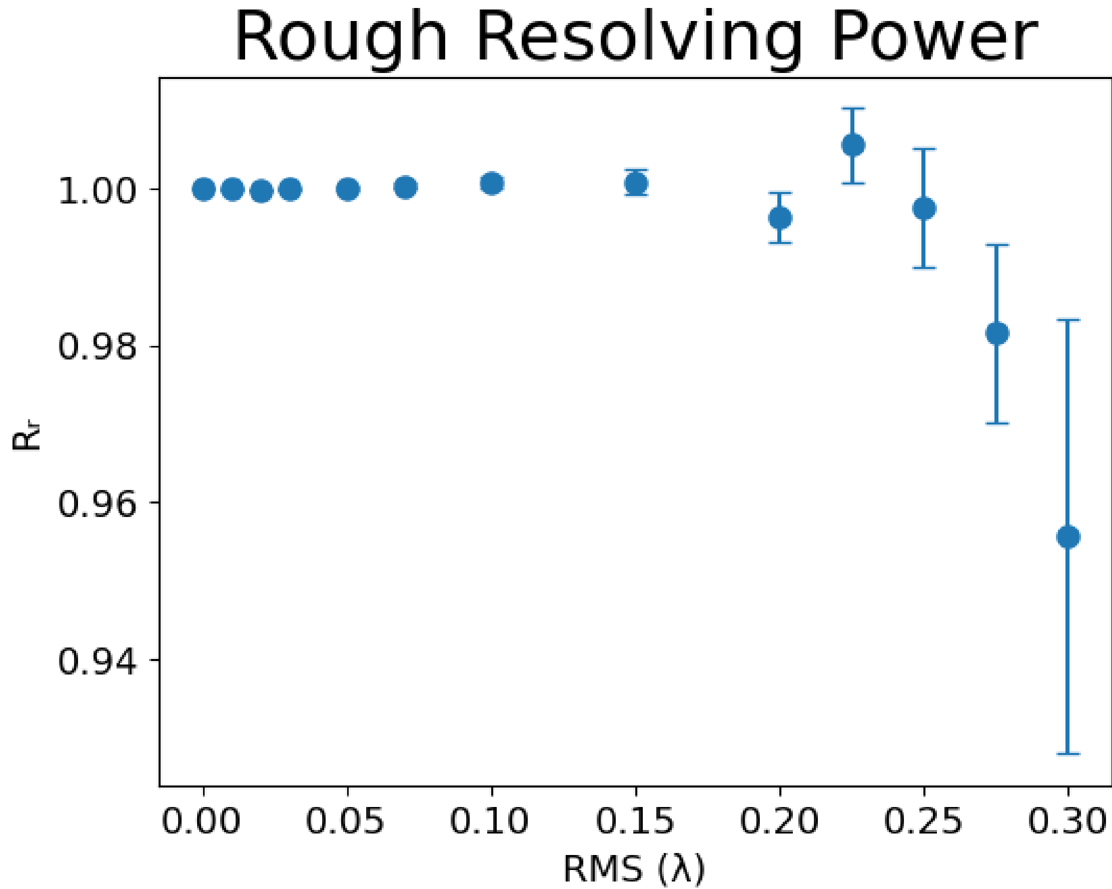

Figure 3.1 Relative resolving power for increasing RMS surface roughness

3.1.1 Surface Roughness

Figure 3.1 shows R_r for a surface with increasing surface roughness. From the graph we can see that R_r decreases as surface roughness increases. If we look at the overlap of uncertainty between adjacent points, though, it is unclear how far R_r drops. Roughness of up to 0.15λ has no observable effect on R_r, and most of the error bars past 0.15λ overlap with the line $R_r = 1.0$. Note that the final data point, $\sigma_r = 0.30\lambda$, which has an average max angle of intensity about 5° off of the first-order diffraction peak, is untrustworthy. Since the code used to calculate R looks for the peak of highest intensity this offset suggests that, at $\sigma_r = 0.30\lambda$, peaks from scattered light are of comparable

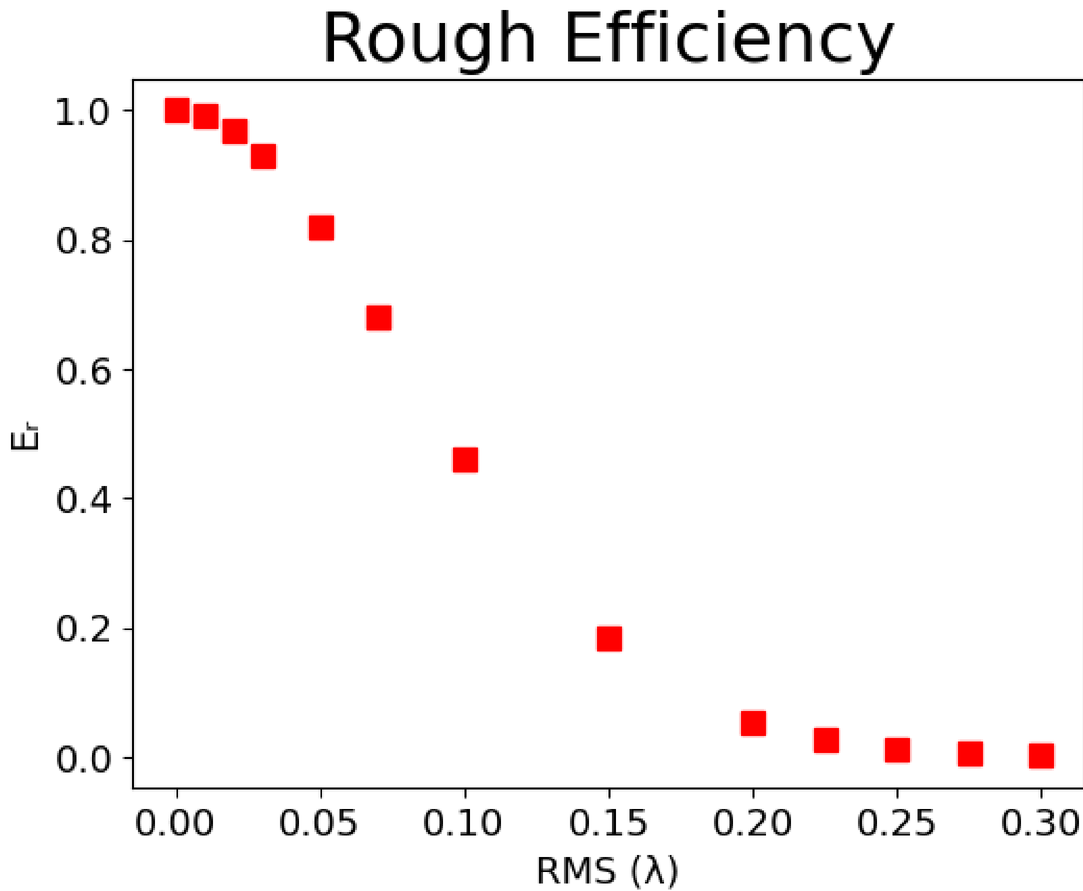

Figure 3.2 Relative efficiency for increasing RMS surface roughness

intensity to those from diffraction. For this reason I did not run tests past $\sigma_r = 0.30\lambda$.

In Figure 3.2 we see a clear decrease in E_r as roughness increases. In fact, the data points seem to follow a Gaussian distribution. At $\sigma_r = 0.2\lambda$, E_r is at about 5.5%; by $\sigma_r = 0.275\lambda$, E_r drops to 0.5%. The SEM for each data point is minuscule, suggesting a clear correlation between efficiency and roughness.

3.1.2 Uncorrelated Ruling Error

Figure 3.3 shows that uncorrelated ruling errors produce even less variation in R_r than surface roughness does. For σ_u values up to 1.0λ, the first-order diffraction peak has the same R value as

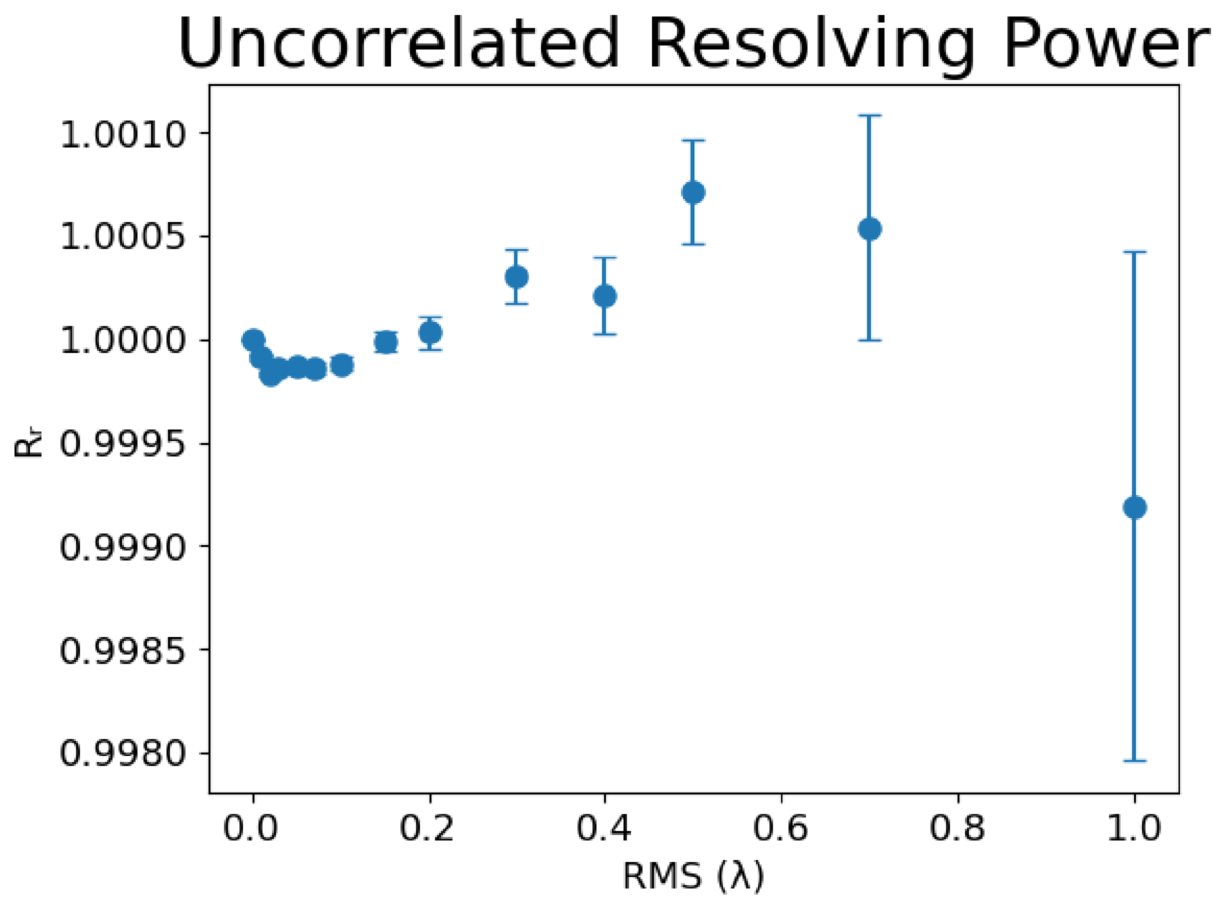

Figure 3.3 Relative resolving power for increasing RMS uncorrelated ruling error

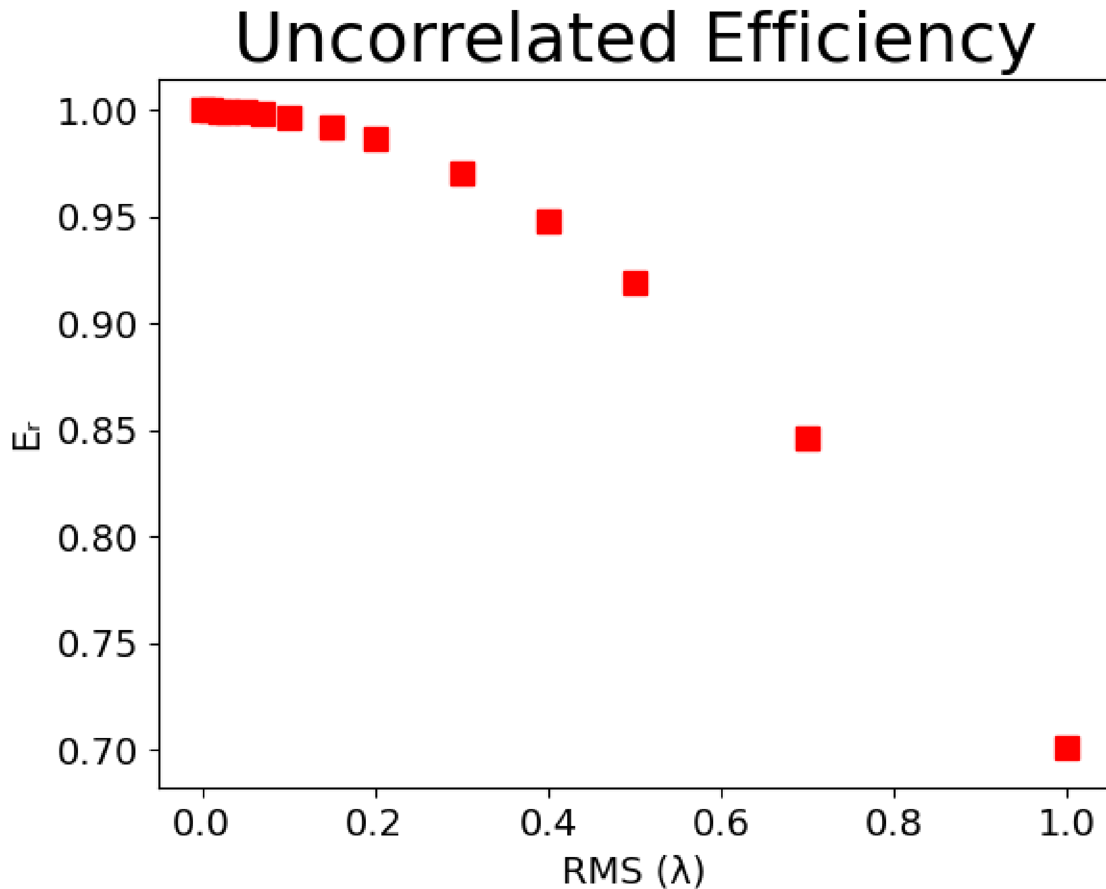

Figure 3.4 Relative efficiency for increasing RMS uncorrelated ruling error

an ideal surface to within 0.1%.

In Figure 3.4 we again see a decrease in E_r as σ_u increases. As in Figure 3.2, the SEM for each data point is imperceptible. Unlike surface roughness, however, uncorrelated ruling errors only cause a steady decrease in E_r. Whereas E_r was practically 0% for $\sigma_r = 0.3\lambda$, for $\sigma_u = 0.3\lambda$ E_r sits at around 96%. Furthermore, the angle of peak intensity for each data point never strays by more than a thousandth of a percent, so each data point accurately represents E_r for the first-order diffraction peak. Perhaps if σ_u extended far past 1.0λ we would see a Gaussian distribution just as in Figure 3.2, but at $\sigma_u = 1.0\lambda$ the RMS error is already about 15% of the ideal groove spacing; larger values of σ_u would be unrealistic.

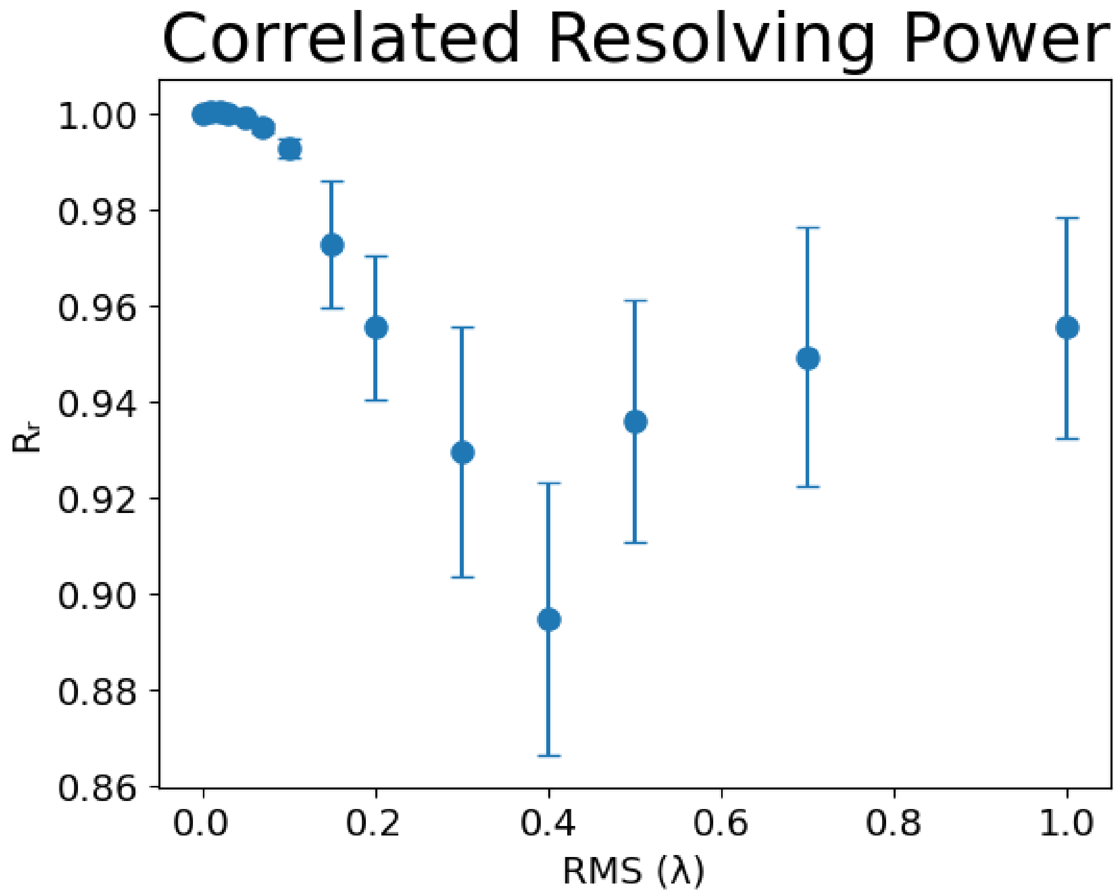

Figure 3.5 Relative resolving power for increasing RMS correlated ruling error

3.1.3 Correlated Ruling Error

As seen in Figure 3.5, correlated ruling errors cause a clear decrease in R_r. This decrease continues through about $\sigma_c = 0.3\lambda$; as error increases past that point, what happens is unclear. The averages indicate a steady increase in R_r, but the uncertainties are large. In fact, the uncertainties for Figure 3.5 are the largest of any figure. It could be that R_r levels off as σ_c increases past 0.3λ, but more samples would need to be taken.

In Figure 3.6, E_r decreases in a manner similar to Figure 3.2, but the change is much more gradual. As σ_c increases to 1.0λ, E_r decreases to 10%.

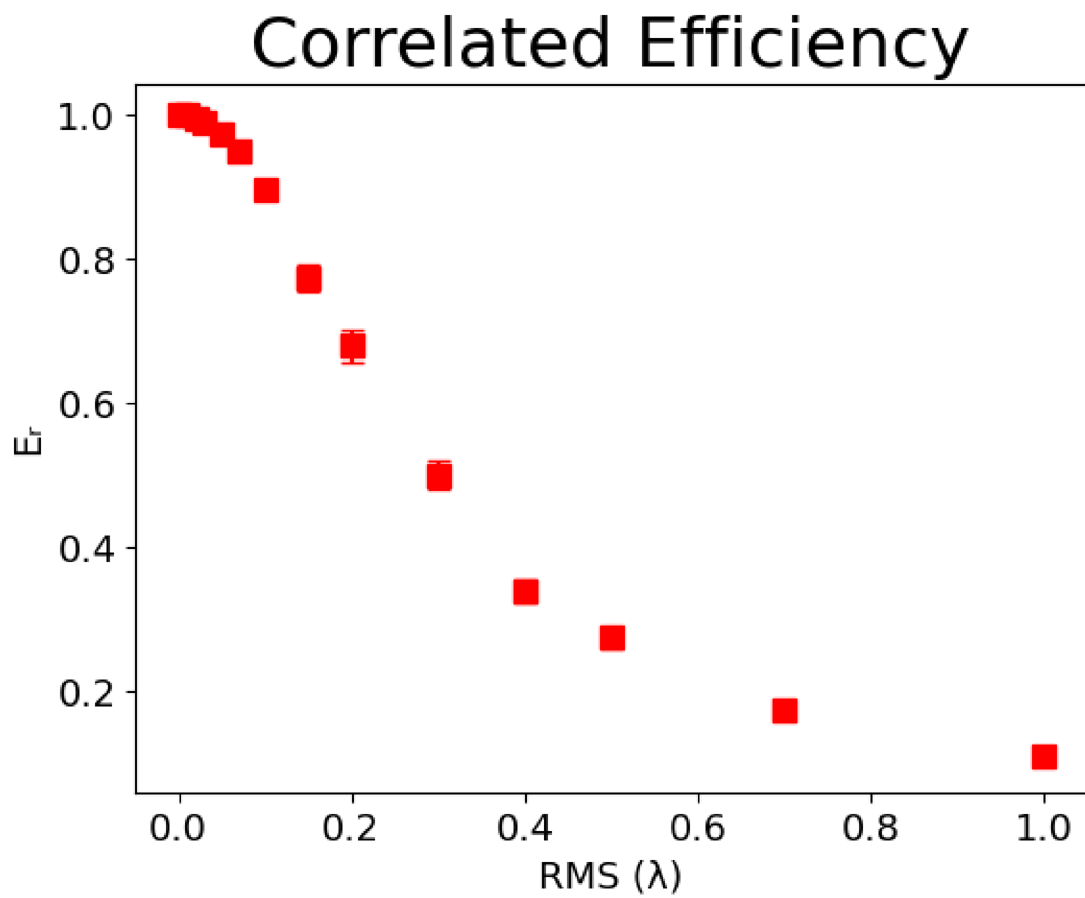

Figure 3.6 Relative efficiency for increasing RMS correlated ruling error

Thresholds for decreasing E			
	σ_r	σ_u	σ_c
5%	$.025\lambda$	0.39λ	0.07λ
10%	$.036\lambda$	0.55λ	0.1λ
20%	$.053\lambda$	0.81λ	0.14λ

Table 3.1 Thresholds for efficiency in λ

3.2 Thresholds

From the data a simple question arises: when should someone care about surface defects of each type, and when are they ignorable? In an attempt to answer this question I will determine threshold values for performance loss of 5%, 10% and 20%. I will first determine these values in units of wavelength. I will then convert into units of nm and apply these results to the EUV.

3.2.1 Thresholds in Wavelengths

Results reveal that surface roughness and uncorrelated ruling errors meet none of the thresholds for performance degradation in the range of values this study considered. Correlated ruling errors do have a significant impact on R, though; a 5% loss occurs at $\sigma_c = 0.23\lambda$ and a 10% loss occurs at $\sigma_c = 0.38\lambda$.

Table 3.1 shows thresholds for decreases in efficiency. All defect types decrease efficiency, which makes sense because each defect reflects light away from the first-order diffraction peak. Roughness has the largest effect because it scatters the most light.

Thresholds for decreasing E (EUV)			
	σ_r	σ_u	σ_c
5%	2.15 nm	33.54 nm	6.02 nm
10%	3.10 nm	47.3 nm	8.60 nm
20%	4.56 nm	69.66 nm	12.04 nm

Table 3.2 Thresholds for efficiency at $\lambda = 86$ nm

3.2.2 Application to EUV

Now that I have found thresholds for performance degradation in units of optical wavelength, I will apply the results to the case of an incident wave in the EUV. I can use the PSDF in Figure 2.3 to pick a reasonable wavelength in nm. Fitting the PSDF in Figure 2.3 with a Gaussian, I found the standard deviation to be about $\sigma = 0.073\text{nm}^{-1}$. When I modeled surface roughness I used a Gaussian filter function with a standard deviation of 2π (in units of optical wavelength) to imitate the spatial frequencies seen in Figure 2.3. In order for the standard deviation in my code to match the standard deviation in Figure 2.3, I need an optical wavelength of

$$\frac{2\pi}{\lambda} = \frac{0.073}{\text{nm}} \tag{3.2}$$

$$\lambda = \frac{2\pi}{0.073}\text{nm} = 86\text{nm} \tag{3.3}$$

With conversions the ideal surface has a groove spacing of $d = 679.4$ nm (about 1470 lines/mm), a realistic spacing for a diffraction grating. With these numbers in place we can see that correlated ruling errors cause a 5% degradation in R at $\sigma_c = 19.78$ nm and a 10% degradation in R at $\sigma_c = 32.68$ nm. Table 3.2 shows thresholds for an incident wavelength of 86 nm. Data from our lab reveals that many thin film surfaces have surface roughness around 2-3 nm–for example, the surface in Figure 2.2 has an RMS roughness of 2.24 nm. If these RMS values are typical for diffraction gratings, then at $\lambda = 86$ nm E_r will be between 90% and 95%.

3.3 Discussion

Referring to Table 3.1, the result that RMS roughness of 0.035λ decreases efficiency by 10% agrees well with a similar study done by a former student. In his thesis, Thevenin found that $\sigma_r = 0.3\lambda$ decreased efficiency by 10% when modeling the effect of roughness on a flat conducting surface [6]. Another interesting observation is the Gaussian distribution in Figure 3.2. This figure corroborates the assumption made by Debye that reflectance may be thought of as a Gaussian distribution centered on an ideal surface and parametrized by surface roughness [5].

The result that surface roughness and uncorrelated ruling errors have little influence on R is also believable because each defect type does not change the overall periodicity of the grating spacing. Diffraction gratings work by summing the diffraction patterns of many equally-spaced grooves (or slits) to create regions of constructive interference. Since roughness doesn't change the location of grooves, it should have little effect on R, as Figure 3.1 shows. Uncorrelated ruling errors do change the spacing of grooves; however, since the location of each groove differs from the ideal case by a random amount, in the limit of many grooves phase changes caused by groove errors in one direction are consistently offset by phase changes from groove errors in the other direction. This is not the case for correlated ruling errors, where the offset in groove locations accumulate across the surface. For correlated ruling errors, a general offset of many grooves undoes the periodicity of the ideal grating surface. Phase changes from dislocated grooves have less chance of being offset by phase changes in an opposite direction, and the resolving power should decrease. The data supports this. Section 3.2 showed that only correlated ruling errors cause significant changes in resolution.

3.4 Future Work

While the results of this study are informative, its scope is limited for many reasons. Limitations include the problem sizes we were able to model, model accuracy, and assumptions that simplified

the math. In the future these limitations may be addressed by increasing computational resources and lowering computational cost, and by decreasing the number of assumptions in our study.

Three factors led to large computational cost. The first and second have to do with the size of the impedance matrix Z. The number of elements in Z depends upon both how large the modeled surface is and how wide each patch should be, where larger surfaces lead to more realistic problems and smaller patch sizes improve the accuracy. The third factor increasing cost is the number of samples run. Running more samples decreases the uncertainty in measuring average performance values, but increases the time of computation. To improve results, one could run more samples of larger surfaces with smaller patches; doing so, however, requires either more resources or faster code. In future studies there are two major steps that could address this issue. The first is to expand computational resources by paralellizing the code. The second step would be to use a multipole expansion of the Green's function to further approximate the far-field reflectance in a way that preserves accuracy . This latter step is particularly promising; preliminary studies by Dr. Turley show an almost tenfold reduction in required storage.

In addition to increasing model sizes and numerical accuracy, including fewer assumptions will make models more realistic. For example, this study only looked at S-polarization. Furthermore this study assumed a perfect conductor, but future studies could model the optical properties of frequently-used materials. The surface I modeled was one-dimensional, which limited the kinds of defects I could study. A two-dimensional surface would allow me to observe other kinds of defects such as angled grooves or grooves with line shifts along a direction perpendicular to the groove spacing. Additionally, by modeling multilayers I could study the effect of interfacial roughness below the surface. Finally, having data about the surface characteristics of actual EUV gratings would allow me to get a much better idea of which manufacturing defects are common and how severe they typically are.

3.5 Conclusion

Using the EFIE, I was able to determine how surface geometry affects the far-field reflection of light from a diffraction grating. Using a model of a one-dimensional blazed grating I studied how surface roughness, uncorrelated ruling errors and correlated ruling errors affect resolving power and efficiency. I found that roughness decreases efficiency most, degrading performance by as much as 20% when σ_r was only about 0.05λ. I found that roughness and uncorrelated ruling errors had little to no effect on resolving power, but that correlated ruling errors of 0.38λ may cause a decrease in resolving power of 10%. Finally, applying these results to the case of an EUV grating with an incident wavelength of 86 nm, I found that RMS roughness of 4.56 nm causes a 20% decrease in efficiency and correlated error of 32.68 nm causes a 10% decrease in resolving power.

Appendix A

Calculating R

Since data about the intensity of reflected light is expressed as a function of observation angle ϕ, it is necessary to convert the width of a peak $\Delta\phi$ to a width $\Delta\lambda$. To do so I will start with Equation 1.7, noting that $\phi = \theta_r$:

$$m\lambda = d(\cos\theta_i + \cos\theta_r) \tag{A.1}$$

Setting m, d, and θ_i as constants, carrying m to the other side and taking derivatives on both sides gives

$$d\lambda = |-\frac{d\sin\theta_r d\theta_r}{m}|, \tag{A.2}$$

where the absolute value is necessary since R is necessarily positive. I will continue by dropping the minus sign. Dividing both sides by λ and inverting I get

$$R \equiv \frac{\lambda}{d\lambda} = \frac{m\lambda}{d\sin\theta_r d\theta_r} \tag{A.3}$$

Equation A.3 is the definition of resolving power in my coordinate system. Setting $m = 1$, $d = 7.9\lambda$, $\theta_r = 125.49^\circ$ and changing the notation from $d\lambda$ to $\Delta\lambda$ gives

$$\frac{\lambda}{\Delta\lambda} = \frac{0.1555}{\Delta\theta_r} \text{ rads} \tag{A.4}$$

or, expressing the answer in milliradians

$$\frac{\lambda}{\Delta\lambda} = \frac{155.5}{\Delta\theta_r} \text{ mrads.} \tag{A.5}$$

The accuracy of Equation A.5 depends on the assumptions that d and θ_r are constant. Due to the nature of my study this is necessarily not always the case, but I can quantify how close Equation A.5 is to what it should be by defining R as a function of d and θ (I will drop the subscript). Let d_i and θ_i denote the spacing of an ideal surface and the first-order diffraction angle of maximum intensity from an ideal surface. By using Equation A.5, the relative error δ is

$$\delta = \left| \frac{R(d,\theta) - R(d_i,\theta_i)}{R(d,\theta)} \right| = \left| 1 - \frac{R_i}{R} \right|. \tag{A.6}$$

Figure A.1 shows where $\delta \leq 1\%$ and Figure A.2 shows where $\delta \leq 5\%$. In all data points from the results section the location of the first-order peak was never off by more than 0.1° (save $\sigma_r = 0.3\lambda$, which was discussed in Section 3.1.1). Therefore the main factor in determining R's accuracy is d. Since groove spacing is preserved when adding surface roughness, Equation A.5 is correct for Figure 3.1. For the other defects d changes from groove to groove; Equation A.5 may not address these cases as well. Currently I do not know whether an average groove spacing for a surface d_{ave} would suffice in Equation A.3 or if another technique for finding $\Delta\lambda$ from $\Delta\theta$ must be developed.

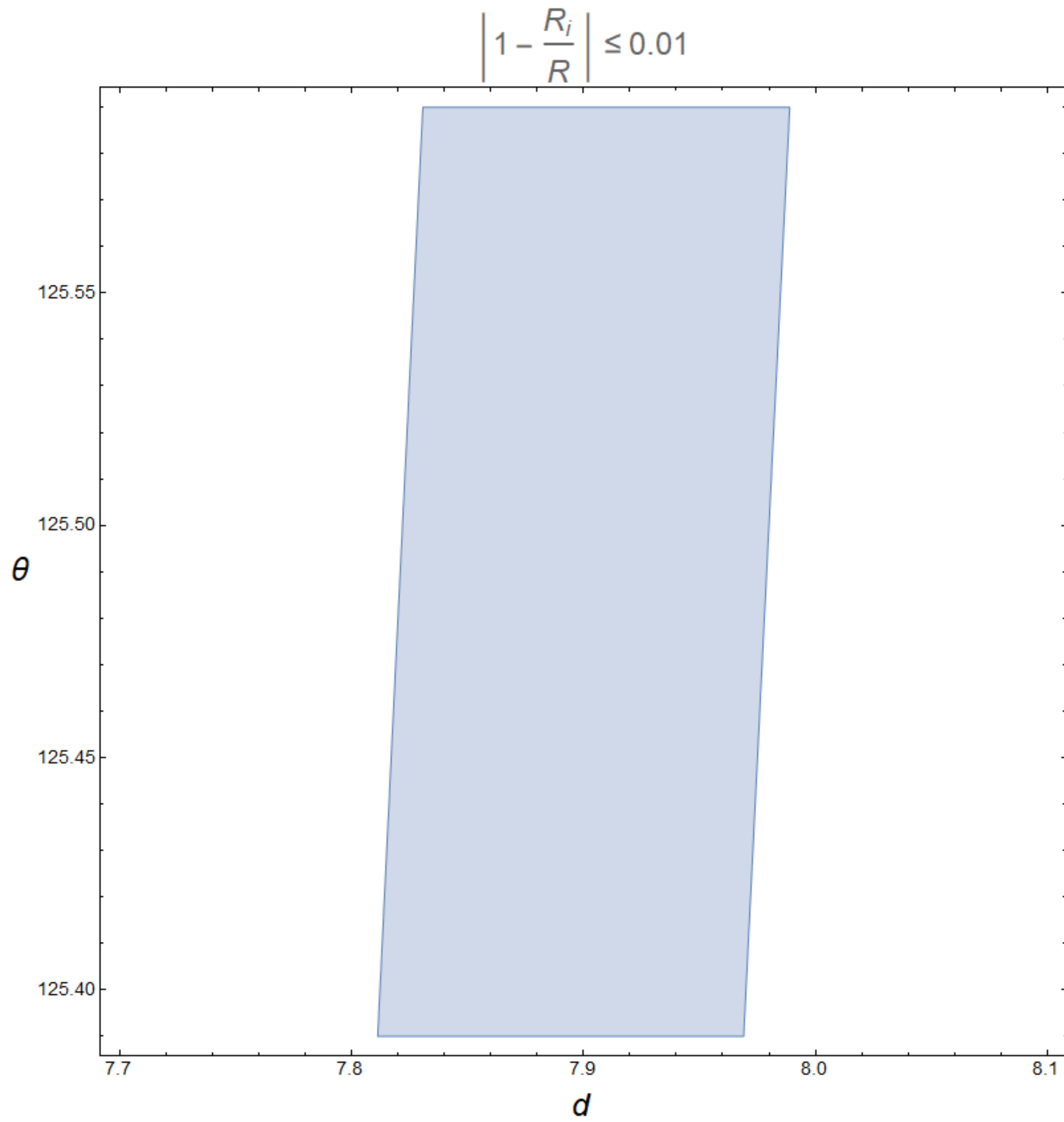

Figure A.1 The blue region represents values of θ (in degrees) and d (in λ) where Equation A.5 is accurate to within 1%.

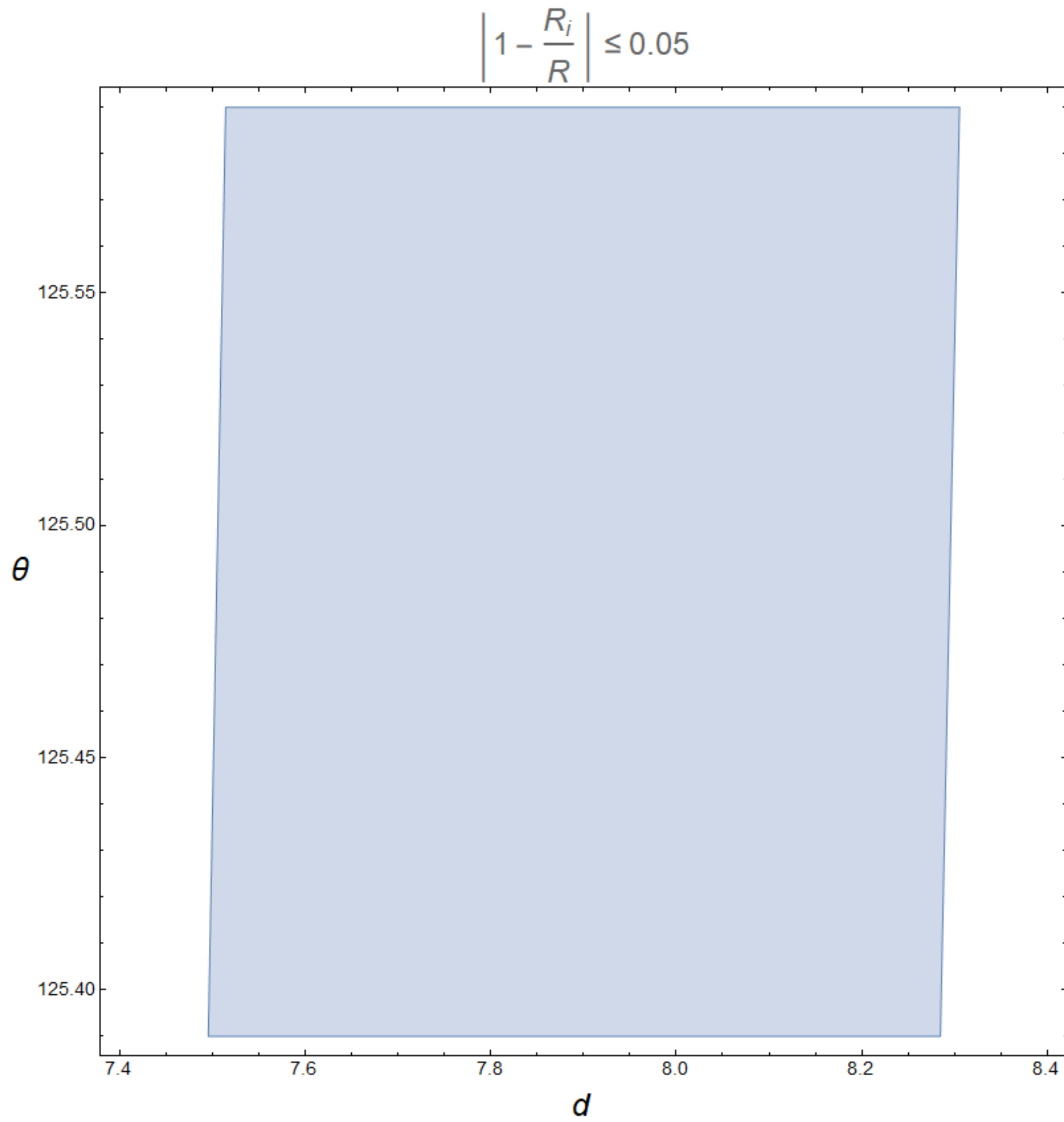

Figure A.2 The blue region represents values of θ (in degrees) and d (in λ) where Equation A.5 is accurate to within 5%.

Appendix B

Choosing the Number of Points Across a Surface

Two concerns which I had to address when choosing the number of points used for a surface model were preserving numerical accuracy and minimizing unwanted diffraction effects. Addressing both concerns requires compromise; larger surfaces require more points and greater accuracy requires greater point density, but both result in higher computational cost. I address both concerns and my compromise in this appendix.

The accuracy of Equation 1.38 is dependent upon the number of patches p used to model a surface. Let surface width be given by w. Then patch width $\ell = \frac{w}{p}$. Since each patch is integrated with a third-order quadrature rule, ℓ needs to be small enough that every patch on a surface is well-approximated with a third-order polynomial. On the other hand, solving Equation 1.38 for J requires computing the inverse of the $4p \times 4p$ matrix Z. As referenced in Section 2.4, Julia uses LU factorization to take Z's inverse. The number of computations required to take the inverse is $O[p^3]$; thus the computational cost scales with the cube of p [12].

Finding a balance required running tests. My advisor Dr. Turley ran the tests included here.

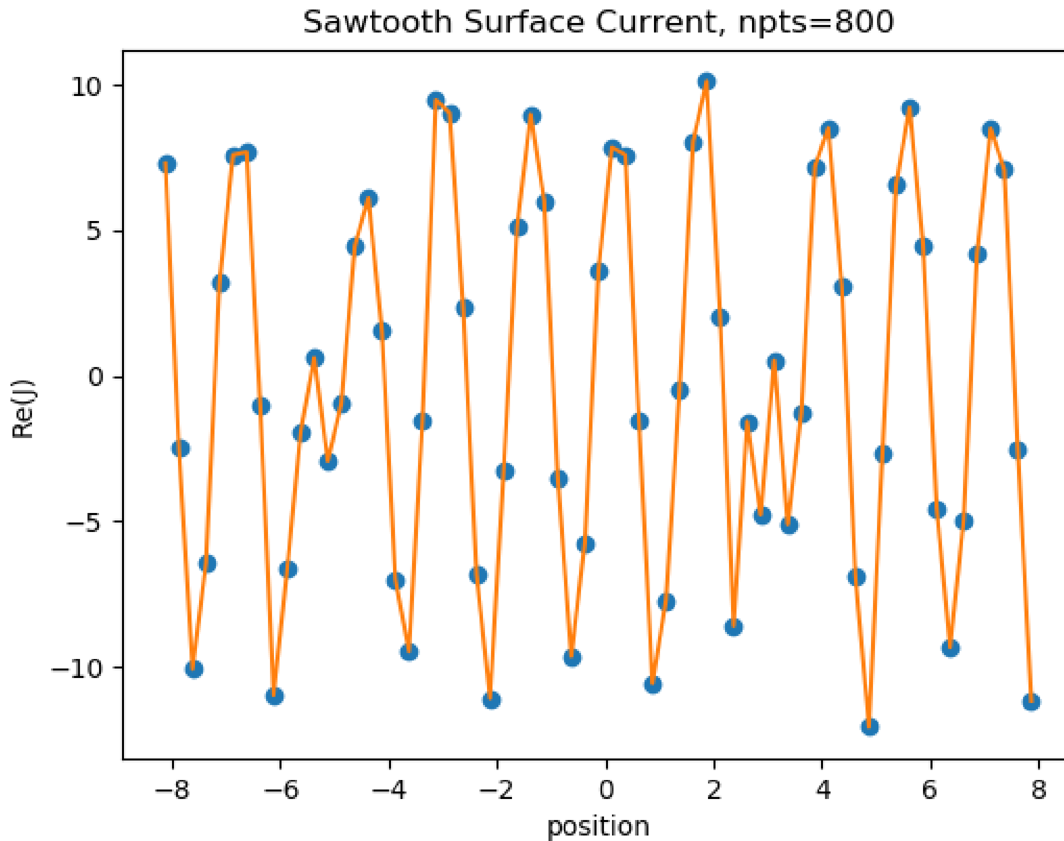

Figure B.1 Real part of J for a blazed grating with four points per wavelength. The dots represent the computed values.

He modeled an ideal blazed grating of width $w = 200\lambda$, groove spacing $d = 7.9\lambda$, and blaze angle $\theta_B = 0.1$ rad. Monochromatic plane-wave light was incident at $\theta_i = 45°$ measured clockwise from grazing. The following plots show computed surface current J along a small portion of the surface. Each dot represents an evaluation points; the lines are to guide the eye. Note that these plots consider points per wavelength rather than patches per wavelength, and I will speak in terms of points per wavelength from here.

Figures B.1 - B.3 show an increasingly detailed surface current as point density increases. At eight points per wavelength you can see discontinuities at each groove along the surface, and at

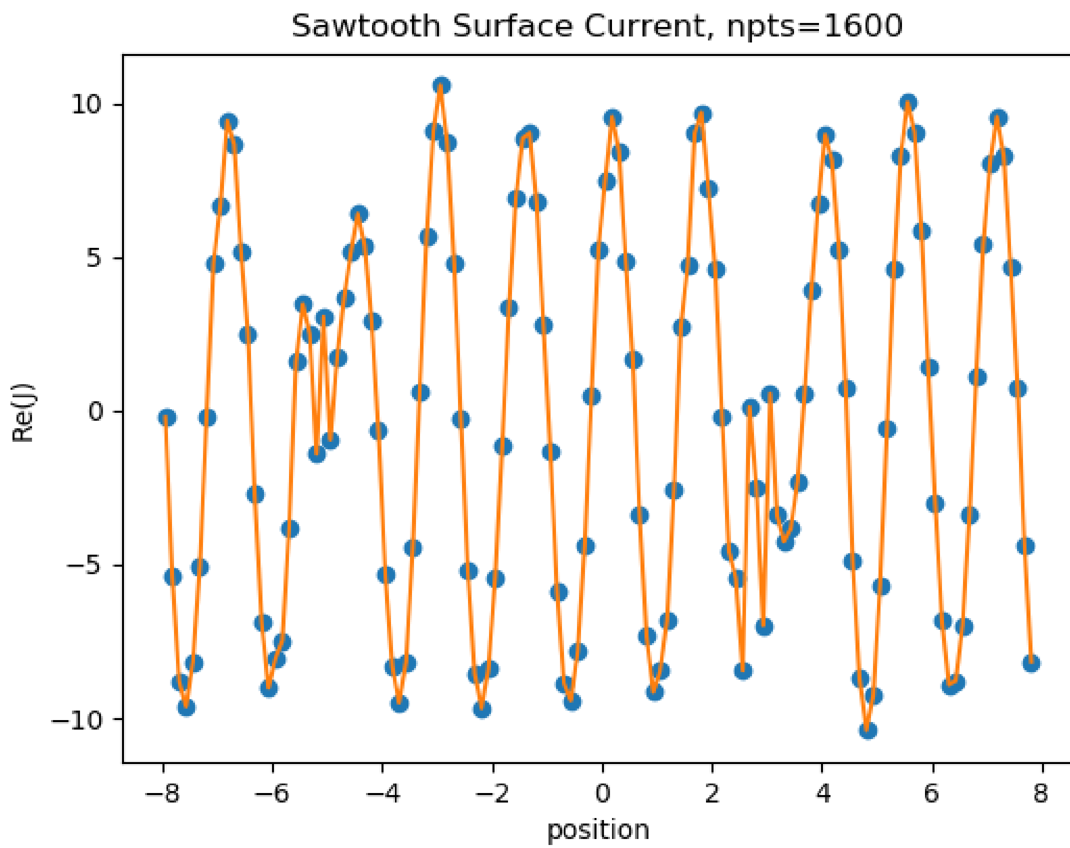

Figure B.2 Real part of J for a blazed grating with eight points per wavelength. The dots represent the computed values.

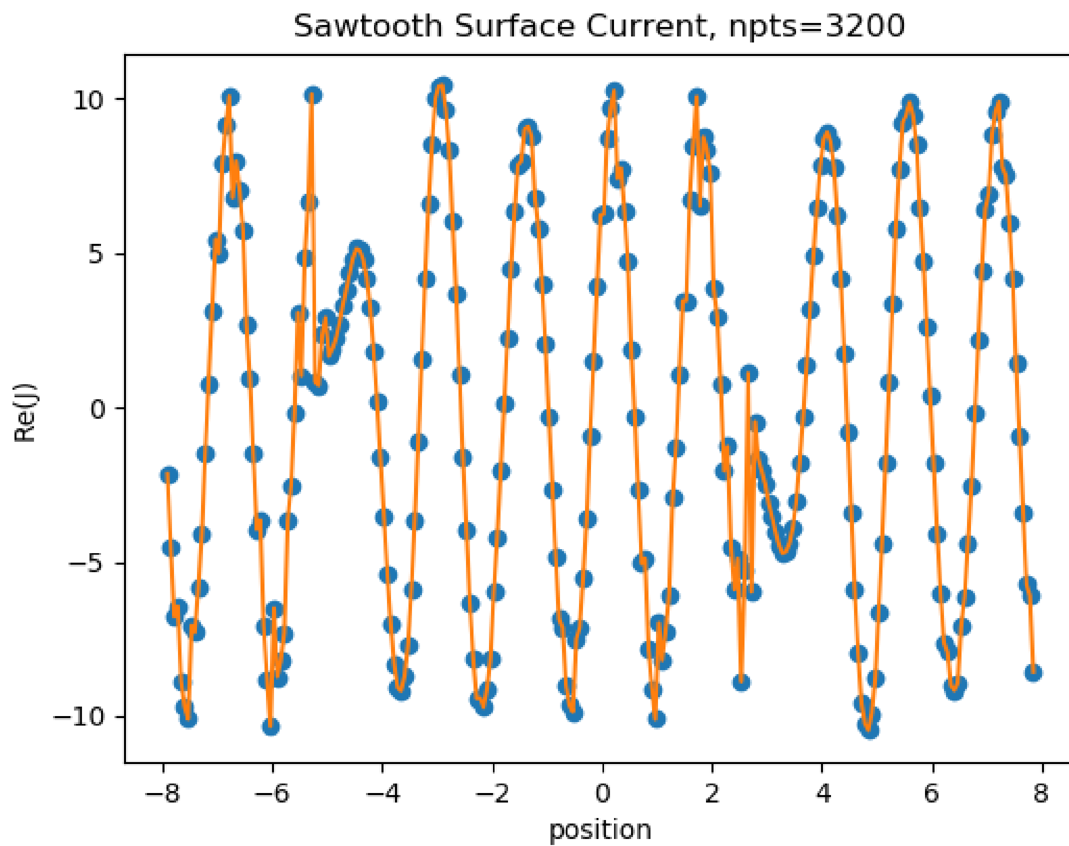

Figure B.3 Real part of J for a blazed grating with sixteen points per wavelength. The dots represent the computed values.

length λ	width (milliradians)
200	5.442
400	2.716
1000	1.084
2000	0.541
3000	0.359
3500	0.380
4000	0.300

Table B.1 First-order peak width. Surfaces were modeled at five points per λ.

sixteen points per wavelength Re$\{J\}$ appears smooth even along grooves.

Another concern was the effect of diffraction . Diffraction is most pronounced when the size of barriers are near the same order of magnitude as an incident wave. As discussed in Section 1.3.1 this is the principle by which diffraction gratings work, but diffraction caused by the width w of the entire grating is unwanted. Table B.1 shows the results of tests run when varying w. Point density was kept at five per wavelength.

In a compromise between accuracy and computational cost, I decided to perform tests with surfaces 1975 wavelengths wide at a point density of ten points per wavelength. This allowed me to model surfaces large enough to minimize diffraction effects while retaining enough accuracy to resolve discontinuities.

Bibliography

[1] V. Holy, J. Kubĕna, I. Ohlídal, K. Lischka, and W. Plotz, "X-ray reflection from rough layered systems," Phys. Rev. B **47,** 15896–15903 (1993).

[2] N. Farnsworth, Senior thesis, "Thorium-based mirrors in the extreme ultraviolet," Brigham Young University, 2005.

[3] D. G. Stearns, "The scattering of x rays from nonideal multilayer structures," Journal of Applied Physics **65,** 491–506 (1989).

[4] Y.-P. Wang, H. Zhou, L. Zhou, R. L. Headrick, A. T. Macrander, and A. S. Özcan, "Interface roughness evolution in sputtered WSi2/Si multilayers.,", 2007.

[5] P. Debye, "Interferenz von Röntgenstrahlen und Wärmebewegung," Annalen der Physik (1913).

[6] S. Thevenin, Senior thesis, "Effects of Roughness on Reflection of Monochromatic Light," Brigham Young University, 2017.

[7] J. E. J. Johnson, Master's thesis, "Computationally Modeling the Effects of Surface Roughness on Soft X-Ray Multilayer Reflectors," Brigham Young University, 2006.

[8] A. F. Peterson, S. L. Ray, and R. Mittra, in *Computational Methods for Electromagnetics* (1998), p. 4.

[9] P. Klapetek, D. Nečas, and C. Anderson, "One-Dimensional Roughness Parameters," http://gwyddion.net/documentation/user-guide-en/roughness-iso.html (Accessed March 15, 2021).

[10] S. L. Miller and D. Childers, "CHAPTER 10 - Power Spectral Density," in *Probability and Random Processes (Second Edition)*, second edition ed., S. L. Miller and D. Childers, eds., (Academic Press, Boston, 2012), pp. 429–471.

[11] "Julia 1.5 Documentation,", Electronic Documentation, 2021, accessed March 2021.

[12] L. N. Trefethen, *Numerical linear algebra* (Society for Industrial and Applied Mathematics, Philadelphia, 1997), pp. 151–152.

Index

coordinates, 14

Debye-Waller factor, 3
diffraction, 4, 43

efficiency, 6
Electric Field Integral Equation (EFIE), 7, 10

Helmholtz equation, 8

Maxwell Equations, 7
multi-pole expansion, 33
multilayers, 3, 33

Nevot-Croce factor, 3

quadrature, 12, 15

resolving power, 6

surface current J, 10